

Frequency Domain Enhanced U-Net for Low-Frequency Information-Rich Image Segmentation in Surgical and Deep-Sea Exploration Robots

Guohao Huo¹, Ruiting Dai¹, Jinliang Liu¹, Ling Shao², Hao Tang^{3,✉}

Abstract—In deep-sea exploration and surgical robotics scenarios, environmental lighting and device resolution limitations often cause high-frequency feature attenuation. Addressing the differences in frequency band sensitivity between CNNs and the human visual system (mid-frequency sensitivity with low-frequency sensitivity surpassing high-frequency), we experimentally quantified the CNN contrast sensitivity function and proposed a wavelet adaptive spectrum fusion (WASF) method inspired by biological vision mechanisms to balance cross-frequency image features. Furthermore, we designed a perception frequency block (PFB) that integrates WASF to enhance frequency-domain feature extraction. Based on this, we developed the FE-UNet model, which employs a SAM2 backbone network and incorporates fine-tuned Hiera-Large modules to ensure segmentation accuracy while improving generalization capability. Experiments demonstrate that FE-UNet achieves state-of-the-art performance in cross-domain tasks such as marine organism segmentation and polyp segmentation, showcasing robust adaptability and significant application potential. The code will be released soon.

I. INTRODUCTION

Image segmentation serves as a foundational task in computer vision, providing critical support for autonomous robotic [1] systems such as surgical robots and deep-sea exploration robots to operate in complex environments. By isolating key features and structural details in images, this technology has demonstrated remarkable potential in cross-domain applications such as marine organism segmentation and polyp segmentation, significantly advancing the development of surgical robotics and deep-sea exploration systems. Although specialized architectures have achieved outstanding performance, critical challenges remain in overcoming low-frequency environments caused by seawater optical attenuation [2] and high-frequency attenuation from surgical electrocoagulation particulates [3], both representing urgent technical bottlenecks.

Deep convolutional neural networks (CNNs) have markedly improved segmentation accuracy, yet their inherent bias toward high-frequency feature learning often leads to suboptimal performance in low-frequency dominant scenarios [4], [5]. For instance, in marine organism segmentation, underwater non-uniform illumination combined with seawater scattering/absorption/refraction induces high-frequency attenuation

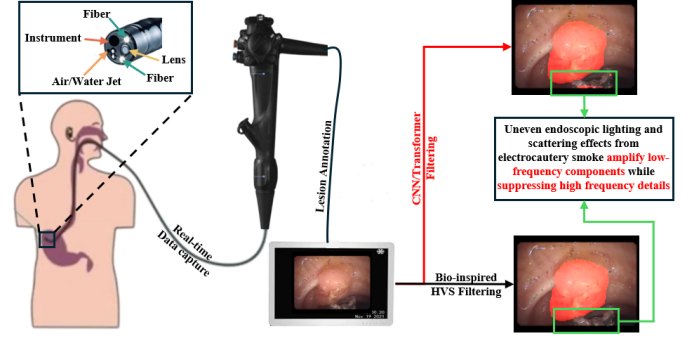


Fig. 1: Under uneven illumination and electrocautery smoke-induced low/high-frequency distortions, compare traditional CNN/Transformer with PFB-equipped FE-UNet for polyp segmentation and lesion localization in the robotic polypectomy endoscopic acquisition and annotation workflow.

[2]. Meanwhile, in polyp segmentation, uneven endoscopic lighting and scattering effects from electrocautery smoke amplify low-frequency effects while suppressing high-frequency details [3], creating precision challenges for robotic surgical systems.

To address these issues, we propose FE-UNet - a novel feature learning framework specifically designed for low-frequency-dominant image segmentation. The framework enhances low-frequency information through Deep Wavelet Convolution (DWTConv) and employs spectral pooling filters to balance frequency components, mimicking the human visual system's mid-frequency sensitivity. The integrated Perception Frequency Block (PFB) with Wavelet-Adaptive Spectral Fusion (WASF) further enables multi-scale feature capture while simulating the receptive field-eccentricity relationship in biological vision. This synergy between CNN capabilities and visual system principles equips deep-sea exploration robots and surgical robots with human-like frequency-aware perception, significantly improving segmentation accuracy under challenging conditions.

During robotic polypectomy procedures, electrocautery-generated smoke scattering and irregular illumination from light guides cause attenuation of high-frequency details and amplification of low-frequency components in the images presented to the display, which severely impairs the ability of conventional CNN/Transformer-based segmentation methods to precisely localize lesions in the input (top right), as shown in Figure 1. Our proposed FE-UNet addresses this by incorporating a bio-inspired Perception Frequency Block (PFB) for frequency-domain enhancement: the WASF module simultaneously strengthens low-frequency cues and balances high- and low-frequency features, and the enhanced

✉Corresponding author

¹Guohao Huo, Ruiting Dai and Jinliang Liu are with the University of Electronic Science and Technology of China. {gh.huo513, rtdai, lualiu510}@gmail.com

²Ling Shao is with the University of Chinese Academy of Sciences. ling.shao@ieee.org

³Hao Tang is with School of Computer Science, Peking University. hao.tang@vision.ee.ethz.ch

representations are then fed to the decoder to produce refined segmentation masks (bottom right). The resulting masks can be fed back to the surgical robot for real-time decision-making such as localization, resection, and sampling.

In summary, our contributions are as follows: (1) We propose FE-UNet, a frequency domain-enhanced segmentation framework designed to improve segmentation performance by enhancing low-frequency feature information in low-quality images and balancing it with high-frequency features. (2) We introduce PFB (Perception Frequency Block), a module that aggregates frequency-domain feature balancing mechanisms, multi-scale receptive fields, and eccentricity-aware features inspired by the human visual system, enabling autonomous robots to acquire human-like visual feature capture capabilities. (3) We develop WASF (Wavelet-Adaptive Spectral Fusion), which strengthens low-frequency information and balances it with high-frequency features, providing a robust foundation for frequency-domain-aware feature learning. (4) Extensive experiments on four marine animal segmentation datasets and five polyp segmentation datasets demonstrate FE-UNet’s state-of-the-art performance, validating its effectiveness in addressing precise segmentation challenges in environments with dominant low-frequency information or attenuated high-frequency details.

II. RELATED WORK

A. Marine Animal Segmentation

Image segmentation technology is crucial for deep-sea exploration robots in marine animal recognition tasks [6], as it enables precise identification in complex underwater environments. In recent years, convolutional neural networks (CNNs) have been widely applied in marine animal segmentation. For instance, [7] proposed an Enhanced Cascaded Decoder Network (ECDNet), while [8] introduced a feature interaction encoder with cascaded decoders to extract more comprehensive features for accurate segmentation in challenging underwater conditions. Similarly, [9] designed a fusion network to learn the semantic features of marine animals.

The Segment Anything Model (SAM) has shown strong segmentation ability. Building on SAM, [10] proposed a dual-SAM with automatic prompting to incorporate rich priors for underwater segmentation, [11] used the SAM encoder for multi-scale features and a progressive prediction framework to capture global underwater information, and [12] applied a U-shaped segmentation framework to improve SAM2 for high-quality marine animal delineation.

However, CNN-based models remain limited by underwater refraction and scattering, which cause loss of high-frequency image features. Because CNNs are sensitive to high-frequency information, their ability to capture semantics is constrained under such frequency-domain distortions from light scattering and absorption.

B. Polyp Segmentation

Polyp segmentation in computer vision focuses on identifying and isolating polyp regions in medical images, which is crucial for surgical robots to recognize and differentiate

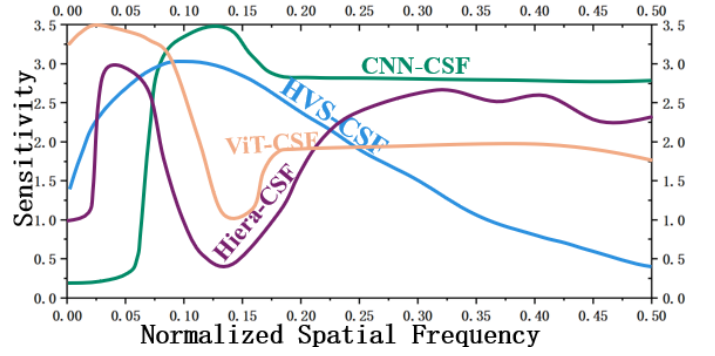


Fig. 2: The Contrast Sensitivity Function model of the human visual system (HVS-CSF) and the Contrast Sensitivity Function model of convolutional neural networks (CNN-CSF), with the horizontal axis representing normalized spatial frequency and the vertical axis representing sensitivity.

polyp lesions from other tissues [13]. The main challenges arise from the diversity of polyp shapes, the ambiguity of their boundaries, and the high similarity between polyps and surrounding tissues. Reference [14] proposed a cross-level feature aggregation network that fuses multi-scale semantic information from different levels to achieve precise segmentation. However, this approach relies solely on convolutional neural networks (CNNs), limiting its ability to capture long-range dependencies within images.

To mitigate this, [15] combined CNNs and Transformers for medical segmentation. However, during surgery low-frequency interference from uneven illumination and electrocautery smoke complicates accurate operation [16], and traditional CNN-/Transformer-based models struggle to capture low-frequency edge and detail information. We propose FE-UNet, which enhances low-frequency features via wavelet transformation for refined segmentation.

C. Frequency Domain Analysis

Frequency-domain analysis has been widely applied in computer vision. Previous works [17], [18] show that low-frequency features in natural images represent global structure and color, while high-frequency features capture edges, textures, and fine details. Studies such as [4], [5] reveal that convolutional neural networks tend to bias toward high-frequency features and underrepresent low-frequency ones, whereas multi-head self-attention favors low-frequency features. WTConv [19] uses wavelet transforms to enhance low-frequency information and enlarge receptive fields. LITv2 [20] proposes the HiLo attention mixer to capture both high- and low-frequency information via self-attention, and SPAM [21] designs a convolutional mixer to balance high- and low-frequency signals.

To the best of our knowledge, no prior work has specifically focused on enhancing low-frequency signals while effectively balancing high- and mid-frequency information. Inspired by this, we propose a novel mixer called Wavelet-Adaptive Spectral Fusion (WASF), which utilizes Deep Wavelet Convolution (DWTConv) to enhance low-frequency signals. Subsequently, spectral pooling filters are applied to the enhanced frequency-domain features to perform frequency mixing, enabling the

effective capture and utilization of high-, mid- and low-frequency information in image representations. In addition, we are the first to propose a method that simulates the human visual system based on frequency information.

III. THE PROPOSED METHOD

A. HVS-CNN Contrast Sensitivity Analysis

The human visual system's ability to discern details is closely related to the relative contrast of the observed area, typically represented by the Contrast Sensitivity Function (CSF) [22]. The CSF is a function of spatial frequency and exhibits a band-pass characteristic. Based on extensive experiments, Mannos and Sakrison proposed a classic model for the Contrast Sensitivity Function:

$$H(f) = 2.6 * (0.192 + 0.114) * e^{[-(0.114f)^{1.1}]}, \quad (1)$$

where the spatial frequency is:

$$f = (f_x^2 + f_y^2)^{0.5}, \quad (2)$$

where f_x and f_y represent the spatial frequencies in the horizontal and vertical directions, respectively, based on this, we plot the contrast sensitivity function (HVS-CSF) curve of the human visual system (see Figure 2). To compare the frequency characteristics of convolutional neural networks, vision Transformers, and Hiera-L in SAM2 with those of the human visual system (HVS), we designed a simple classification experiment. The experiment uses the CIFAR-10 dataset [23]. We performed classification inference with ResNet18, ViT-B, and Hiera-L models pretrained on ImageNet. To analyze the sensitivity of CNN, ViT, and Hiera-L feature maps to information at different frequencies, we applied the following operations sequentially to each channel of the feature maps.

$$\begin{aligned} F(u, v) &= \int_{-\infty}^{\infty} \int_{-\infty}^{\infty} f(x, y) e^{-2\pi i(ux+vy)} dx dy, \\ M(u, v) &= \begin{cases} 1 & \text{if } r \leq R; \\ 0 & \text{if } r > R. \end{cases} \end{aligned} \quad (3)$$

Filter the image with different cutoff frequencies and then apply the inverse Fourier transform.

$$f_{\text{filtered}}(x, y) = \int_{-\infty}^{\infty} \int_{-\infty}^{\infty} F_{\text{filtered}}(u, v) e^{2\pi i(ux+vy)} du dv, \quad (4)$$

Convert the frequency-domain features back to the spatial domain and then measure the model's classification accuracy at different cutoff frequencies. Plot the contrast sensitivity function curves for CNN, Transformer, and Hiera-L (CNN-CSF, ViT-CSF, and Hiera-CSF) in Figure 2. We can draw the following conclusions:

- 1) The human visual system is most sensitive to mid-frequency signals, with lower sensitivity to both low-frequency and high-frequency signals.
- 2) Convolutional neural networks exhibit low sensitivity to low-frequency signals. They are more responsive to mid-to-high-frequency signals, with a slightly greater

sensitivity to mid-frequency signals compared to high-frequency signals.

- 3) ViT is more sensitive to low-frequency signals than to high-frequency signals, while it has relatively low sensitivity to mid-frequency signals.
- 4) Hiera-L shows roughly consistent sensitivity to low- and high-frequency signals, lying between CNNs and ViT in that respect, but it has extremely low sensitivity to mid-frequency signals.

Based on this, we propose the wavelet adaptive spectral fusion (WASF), which enhances low-frequency signals using a DWTConv. This is followed by mixing operations with a spectral pooling filter to blend high-frequency and low-frequency signals into the mid-frequency range, fully leveraging the convolutional module's high sensitivity to mid-frequency signals.

To further simulate the human visual system, we propose the Perceptual Frequency Block (PFB). This module combines frequency domain information enhancement with the relationship between receptive field and eccentricity in the human visual system, achieving a more accurate simulation of the visual perception mechanism. Building on the PFB, the Hiera-L Block, and a U-shaped architecture, we have innovatively developed the FE-UNet architecture.

B. FE-UNet

The original SAM2 model generates segmentation results that are class-agnostic. Without manual prompts for specific classes, SAM2 cannot produce segmentation results for designated categories. To enhance the specificity of SAM2 and better adapt it to specific downstream tasks while efficiently using pre-trained parameters, we propose the FE-UNet architecture (as shown in Figure 3(a)). The architecture demonstrates robust segmentation capabilities for low-resolution images.

Encoder. FE-UNet leverages the pre-trained Hiera-L backbone network from SAM2. The attention mechanisms within the Hiera backbone address the limitations of traditional convolutional neural networks in capturing long-range contextual features. Furthermore, the hierarchical structure of the Hiera module facilitates the capture of multi-scale features, making it well-suited for designing U-shaped networks.

To achieve parameter-efficient fine-tuning, we design task-specific Res-Adapter and Mlp-Adapter with trainable parameters within the Hiera Block while keeping the parameters of the Hiera Block frozen. This approach eliminates the need to fine-tune the Hiera Block, significantly reducing memory consumption.

Res-Adapter. We designed the Res-Adapter following [24], [25]: a downsampling linear layer, GeLU activation, and an upsampling linear layer. Parameters are initialized to zero so the Adapter can fine-tune attention outputs while keeping changes small. We add residual connections to avoid gradient vanishing from zero initialization. This yields efficient Hiera Block fine-tuning with minimal memory overhead.

Mlp-Adapter. Inspired by [26], [27], we propose Mlp-Adapter, a lightweight MLP module that runs in parallel with

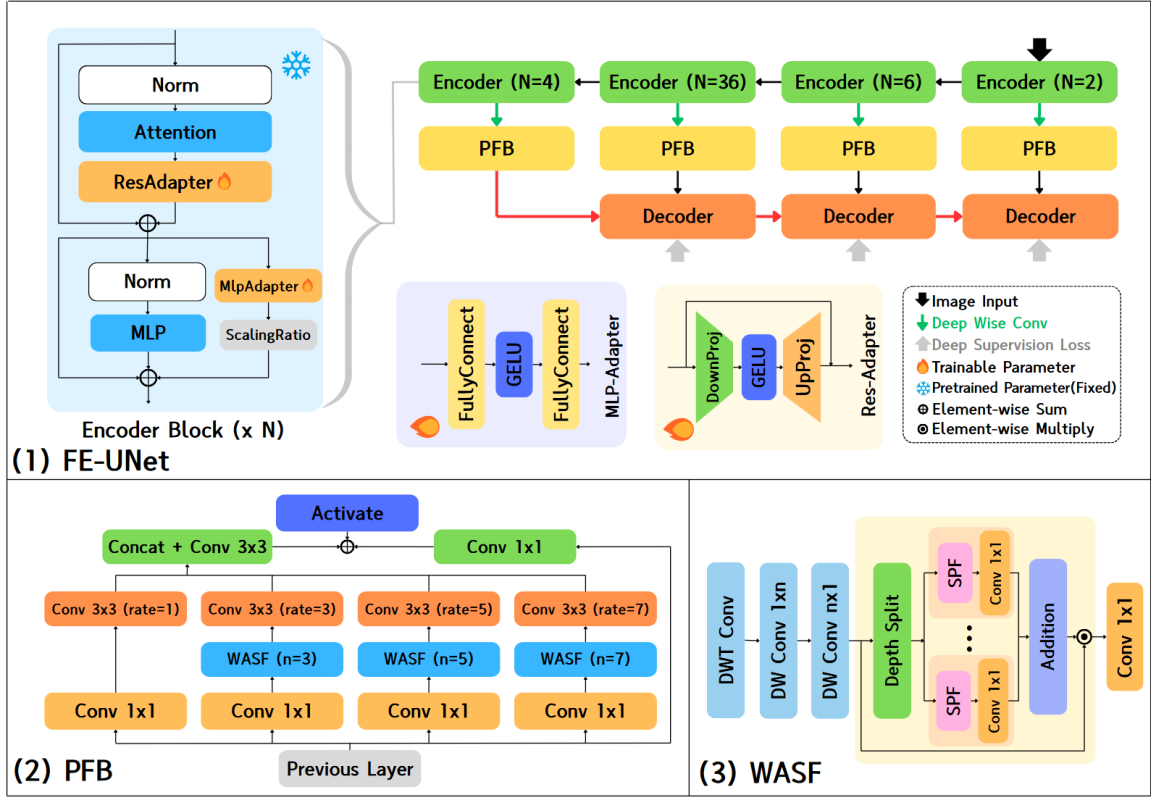


Fig. 3: Fig. (a), (b), and (c) depict the architectures of the proposed FE-UNet model, Perception Frequency Block (PFB), and Wavelet-Adaptive Spectral Fusion (WASF), respectively.

the pretrained MLP and residual connections. It preserves backbone information flow while efficiently enhancing task-specific semantic relationships and nonlinear feature interactions, improving feature refinement with minimal memory overhead.

PFB. After encoder feature extraction, the U-shaped network’s hierarchical features are fused via depthwise convolution, reducing channels to 64 to lower GPU memory for the following Perceptual Frequency Block (PFB). The fused features are then processed by the PFB, which simulates characteristics of the human visual system while emphasizing feature enhancement in the frequency domain.

Decoder. We made adjustments to the decoder part of the traditional UNet architecture, using the same upsampling operations. However, we implemented a customized DoubleConv module, which consists of two identical convolution—batch normalization—ReLU activation function combinations. The convolution operations use a kernel size of 3×3 . Each decoder output feature is processed through a 1×1 convolutional segmentation head to generate segmentation results $S_i (i \in \{1, 2, 3\})$. These segmentation results are then upsampled and supervised against the ground truth segmentation masks.

Loss Function. Each hierarchical structure loss function in FE-UNet is composed of a weighted Intersection over Union (IoU) and Binary Cross-Entropy (BCE) loss. The specific single-level loss function is defined as follows:

$$L = L_{IoU}^w + L_{BCE}^w. \quad (5)$$

Since we employ deep supervision, the final loss function for FE-UNet is expressed as the sum of the individual hierarchical losses:

$$L_{total} = \sum_{i=1}^3 L(G, S_i). \quad (6)$$

C. PFB

The human visual system’s ability to capture semantic information in natural images varies across different frequency domains. Generally, the human visual system (HVS) is most sensitive to mid-frequency signals, with higher sensitivity to low-frequency signals compared to high-frequency ones.

We employ Wavelet-Adaptive Spectral Fusion (WASF) to enhance low-frequency components in image features while performing adaptive fusion operations with high-frequency information. This process shifts the frequency characteristics of image features toward the mid-frequency range, thereby achieving simulation effects that simulate the receptive fields and eccentricity mechanisms of the human visual system. It also enhances the ability of subsequent convolutional operations to extract feature information.

To achieve multi-scale receptive field capture, we employ the wavelet-adaptive spectral fusion (WASF) with different depths and convolution kernel sizes. In the WASF, n represents the radius size of the low-frequency region A^{lf} centered at the origin, which is 2^n . The depth convolution part of the WASF is configured with kernel sizes of $1 \times n$ and $n \times 1$.

Subsequently, the padding numbers and dilation rates for the different branches of the dilated convolutions are set to $rate = 1, 3, 5, 7$. This configuration facilitates expansion of the receptive field and aligns the feature sizes, making it convenient for subsequent concatenation operations. As a result, we propose the PFB, with the structural diagram illustrated in Figure 3(b).

D. WASF

In the field of computer vision, two common image filtering methods are used: one involves kernel convolution in the spatial domain, while the other utilizes the Fourier transform for filtering in the frequency domain. The method proposed in this paper operates in the frequency domain, but to achieve simple and efficient deep aggregation of spectral information under different receptive fields, we employ wavelet filtering. By applying a multi-branch spectral pooling filter followed by mixing operations on the Deep Wavelet Convolution (DWTConv), we introduce the Wavelet-Adaptive Spectral Fusion (WASF). The module architecture is shown in Figure 3(c).

DWTConv. To fully exploit low-frequency features, we employ cascaded deep-wavelet convolution operations. Similar to the WTConv approach (Reference [19]), we only adjusted the number of channels to 1.

SPF. Based on the inverse power law, the most important visual information in natural images is concentrated in the mid-frequency region. After using the DWTConv, we employ spectral pooling filters to perform mixing operations on the low-frequency and high-frequency components in the spectrum, thereby increasing the weight of the low-frequency components. First, we use a two-dimensional DFT to map the features obtained after deep convolution from the spatial domain to the frequency domain:

$$Z = \mathcal{F}(z) \in \mathbb{C}^{H \times W}. \quad (7)$$

In the above formula, $\mathcal{F}(\cdot)$ represents the two-dimensional DFT operation. Next, we perform a shifting operation to move the low-frequency components to the center of the spectrum. We then use a Fourier transform centering function to remove the remaining parts outside of the low-frequency subset.

$$S^{lf} = \begin{cases} \mathcal{G}(Z)(u, v), & \text{if } (u, v) \in \mathbf{A}^{lf} \\ 0, & \text{else} \end{cases} \quad (8)$$

In the above formula, $\mathcal{G}(\cdot)$ is the Fourier transform centering function, (u, v) is a pair of positions in the frequency domain, and $\mathbf{A}^{lf} \in \mathbb{R}^2$ represents the low-frequency region centered at the origin.

High-pass filters are the opposite of low-pass filters, so high-frequency components can be directly obtained by removing low-frequency components from the input feature map:

$$S^{hf} = \mathcal{G}(Z) - S^{lf}. \quad (9)$$

Finally, by sequentially applying the inverse transformation and inverse DFT operation to the high-frequency and low-frequency components, we can obtain the spectral pooled

feature map:

$$f_{lp}(Z) = \mathcal{F}^{-1}(\mathcal{G}^{-1}(S^{lf})) \in \mathbb{R}^{H \times W}, \quad (10)$$

$$f_{hp}(Z) = \mathcal{F}^{-1}(\mathcal{G}^{-1}(S^{hf})) \in \mathbb{R}^{H \times W}. \quad (11)$$

We mix the visual features of different frequency bands obtained from the decomposition using a combination filter, which can be represented by the following formula:

$$\tilde{Z} = \lambda f_{lp}(Z) + (1 - \lambda) f_{hp}(Z) \in \mathbb{R}^{H \times W}. \quad (12)$$

Since $\mathcal{F}(\cdot)$ and $\mathcal{G}(\cdot)$, as well as their inverses, are linear operations, they satisfy the principle of superposition. The above formula is equivalent to:

$$\tilde{Z} = \mathcal{F}^{-1}(\mathcal{G}^{-1}(\lambda S^{lf} + (1 - \lambda) S^{hf})), \quad (13)$$

where $\lambda \in [0, 1]$ is a balancing parameter. We can now manipulate the frequency spectrum of visual features by adjusting λ to control the balance between the high-frequency and low-frequency components.

IV. EXPERIMENTS

A. Datasets and Evaluation Metrics.

Following the convention [46], [21], we experimentally validated the effectiveness of FE-UNet on two tasks: marine animal segmentation and polyp segmentation.

Marine Animal Segmentation Deep-sea exploration robots are tasked with separating marine animals from their deep-sea environments to analyze biodiversity and protect endangered species. However, during operations, high-frequency attenuation caused by the combined effects of underwater non-uniform illumination and seawater scattering/absorption/refraction poses challenges. To evaluate our model's performance in low-frequency information-rich deep-sea environments, we employed four public benchmark datasets: MAS3K, RMAS, UFO120, and RUWI datasets.

Polyp Segmentation Polyp segmentation aims to accurately delineate polyp regions in endoscopic images, supporting early colorectal cancer screening and intraoperative decisions. In robotic polypectomy, segmentation is challenged by wide variation in polyp shape and size, low contrast with surrounding mucosa, and imaging degradations—such as instrument motion, endoscope shake, uneven illumination, and electrocautery smoke—that cause blur and scatter, suppress high-frequency details, and complicate boundary localization. To assess robustness and clinical applicability under these conditions, we validated the proposed model on five public benchmarks: Kvasir-SEG, CVC-ClinicDB, CVC-ColonDB, CVC-300, and ETIS, which cover diverse polyp types, acquisition settings, and degradation modes, providing a rigorous testbed for weak-texture, low-contrast, and motion-artifact scenarios.

For the marine animal segmentation task, we employed five evaluation metrics—mean Intersection over Union (mIoU), S-measure (S_α), weighted F-measure (F_β^w), mean E-measure (mE_ϕ), and mean absolute error (MAE)—to assess model performance. In the polyp segmentation task, model effectiveness was evaluated using two key metrics: mean Dice

TABLE I: Marine animal segmentation performance on MAS3K, RMAS, UFO120 and RUWI datasets.

Category	Method	MAS3K					RMAS					UFO120					RUWI				
		mIoU	S _α	F _β ^w	mE _φ	MAE	mIoU	S _α	F _β ^w	mE _φ	MAE	mIoU	S _α	F _β ^w	mE _φ	MAE	mIoU	S _α	F _β ^w	mE _φ	MAE
CNN	PfANet [28]	0.405	0.690	0.471	0.768	0.086	0.556	0.767	0.582	0.810	0.051	0.677	0.752	0.723	0.815	0.129	0.773	0.765	0.811	0.867	0.096
	SCRN [29]	0.693	0.839	0.730	0.869	0.041	0.695	0.842	0.731	0.878	0.030	0.678	0.783	0.760	0.839	0.106	0.830	0.847	0.883	0.925	0.059
	UNet++ [30]	0.506	0.726	0.552	0.790	0.083	0.558	0.763	0.644	0.835	0.046	0.412	0.459	0.433	0.451	0.409	0.586	0.714	0.678	0.790	0.145
	U2Net [31]	0.654	0.812	0.711	0.851	0.047	0.676	0.830	0.762	0.904	0.029	0.680	0.792	0.709	0.811	0.134	0.841	0.873	0.861	0.786	0.074
	SINet [32]	0.658	0.820	0.725	0.884	0.039	0.684	0.835	0.780	0.908	0.025	0.767	0.837	0.834	0.890	0.079	0.785	0.789	0.825	0.872	0.096
	BASNet [33]	0.677	0.826	0.724	0.862	0.046	0.707	0.847	0.771	0.907	0.032	0.710	0.809	0.793	0.865	0.097	0.841	0.871	0.895	0.922	0.056
	PFNet [34]	0.695	0.839	0.746	0.890	0.039	0.694	0.843	0.771	0.922	0.026	0.570	0.708	0.550	0.683	0.216	0.864	0.883	0.870	0.790	0.062
	RankNet [35]	0.658	0.812	0.722	0.867	0.043	0.704	0.846	0.772	0.927	0.026	0.739	0.823	0.772	0.828	0.101	0.865	0.886	0.889	0.759	0.056
	C2FNet [36]	0.717	0.851	0.761	0.894	0.038	0.721	0.858	0.788	0.923	0.026	0.747	0.826	0.806	0.878	0.083	0.840	0.830	0.883	0.924	0.060
	ECDNet [7]	0.711	0.850	0.766	0.901	0.036	0.664	0.823	0.689	0.854	0.036	0.693	0.783	0.768	0.848	0.103	0.829	0.812	0.871	0.917	0.064
	OCENet [37]	0.667	0.824	0.703	0.868	0.052	0.680	0.836	0.752	0.900	0.030	0.605	0.725	0.668	0.773	0.161	0.763	0.791	0.798	0.863	0.115
	ZoomNet [38]	0.736	0.862	0.780	0.898	0.032	0.728	0.855	0.795	0.915	0.022	0.616	0.702	0.670	0.815	0.174	0.739	0.753	0.771	0.817	0.137
	MASNet [9]	0.742	0.864	0.788	0.906	0.032	0.731	0.862	0.801	0.920	0.024	0.754	0.827	0.820	0.879	0.083	0.865	0.880	0.913	0.944	0.047
	SETR [39]	0.715	0.855	0.789	0.917	0.030	0.654	0.818	0.747	0.933	0.028	0.711	0.811	0.796	0.871	0.089	0.832	0.864	0.895	0.924	0.055
Trans.	TransUNet [40]	0.739	0.861	0.805	0.919	0.029	0.688	0.832	0.776	0.941	0.025	0.752	0.825	0.827	0.888	0.079	0.854	0.872	0.910	0.940	0.048
	H2Former [15]	0.748	0.865	0.810	0.925	0.028	0.717	0.844	0.799	0.931	0.023	0.780	0.844	0.845	0.901	0.070	0.871	0.884	0.919	0.945	0.045
SAM	SAM [41]	0.566	0.763	0.656	0.807	0.059	0.445	0.697	0.534	0.790	0.053	0.681	0.768	0.745	0.827	0.121	0.849	0.855	0.907	0.929	0.057
	Med-SAM [42]	0.739	0.861	0.811	0.922	0.031	0.678	0.832	0.778	0.920	0.027	0.774	0.842	0.839	0.899	0.072	0.877	0.885	0.921	0.942	0.045
	SAM-Adapter [43]	0.714	0.847	0.782	0.914	0.033	0.656	0.816	0.752	0.927	0.027	0.757	0.829	0.834	0.884	0.081	0.867	0.878	0.913	0.946	0.046
	SAM-DADF [44]	0.742	0.866	0.806	0.925	0.028	0.686	0.833	0.780	0.926	0.024	0.768	0.841	0.836	0.893	0.073	0.881	0.889	0.925	0.940	0.044
	I-MedSAM [45]	0.698	0.835	0.759	0.889	0.039	0.633	0.803	0.699	0.893	0.035	0.730	0.818	0.788	0.865	0.084	0.844	0.849	0.897	0.923	0.050
	Dual-SAM [10]	0.799	0.884	0.838	0.933	0.023	0.735	0.860	0.812	0.944	0.022	0.810	0.856	0.864	0.914	0.064	0.904	0.903	0.939	0.959	0.035
	MAS-SAM [11]	0.788	0.887	0.840	0.938	0.025	0.742	0.865	0.819	0.948	0.021	0.807	0.861	0.864	0.914	0.063	0.902	0.894	0.941	0.961	0.035
	SAM2-UNet [12]	0.799	0.903	0.848	0.943	0.021	0.738	0.874	0.810	0.944	0.022	0.810	0.858	0.845	0.889	0.072	0.906	0.903	0.927	0.941	0.037
	FE-UNet (Ours)	0.815	0.900	0.848	0.928	0.022	0.758	0.874	0.811	0.938	0.021	0.821	0.871	0.856	0.914	0.067	0.914	0.912	0.936	0.959	0.037

score (mDice) and mIoU. Detailed implementation details and dataset configurations are provided in the Supplementary Material.

B. Comparison with State-of-the-Arts.

In this section, we compare our method with other approaches on four public marine animal segmentation datasets and five public polyp segmentation datasets. The quantitative and qualitative results clearly demonstrate the significant advantages of our proposed method.

TABLE II: Polyp segmentation performance on Kvasir-SEG [47], CVC-ClinicDB [48], CVC-ColonDB [49], CVC-300 [50], and ETIS [51] datasets.

Method	Kvasir	ClinicDB	ColonDB	CVC-300	ETIS
	mDice mIoU	mDice mIoU	mDice mIoU	mDice mIoU	mDice mIoU
UNet [52]	0.818 0.746	0.823 0.755	0.504 0.436	0.710 0.627	0.398 0.335
SFA [53]	0.723 0.611	0.700 0.607	0.456 0.337	0.467 0.329	0.297 0.217
UNet++ [30]	0.821 0.744	0.794 0.729	0.482 0.408	0.707 0.624	0.401 0.344
PraNet [54]	0.898 0.840	0.899 0.849	0.709 0.640	0.871 0.797	0.628 0.567
EU-Net [55]	0.908 0.854	0.902 0.846	0.756 0.681	0.837 0.765	0.687 0.609
SANet [56]	0.904 0.847	0.916 0.859	0.752 0.669	0.888 0.815	0.750 0.654
MSNet [57]	0.905 0.849	0.918 0.869	0.751 0.671	0.865 0.799	0.723 0.652
C2FNet [36]	0.886 0.831	0.919 0.872	0.724 0.650	0.874 0.801	0.699 0.624
MSEG [58]	0.897 0.839	0.909 0.864	0.735 0.666	0.874 0.804	0.700 0.630
DCRNet [59]	0.886 0.825	0.896 0.844	0.704 0.631	0.856 0.788	0.556 0.496
LDNet [60]	0.887 0.821	0.881 0.825	0.740 0.652	0.869 0.793	0.645 0.551
FAPNet [61]	0.902 0.849	0.925 0.877	0.731 0.658	0.893 0.826	0.717 0.643
ACSNet [62]	0.898 0.838	0.882 0.826	0.716 0.649	0.863 0.787	0.578 0.509
H2Former [15]	0.910 0.858	0.922 0.871	0.719 0.642	0.856 0.793	0.614 0.547
CaraNet [63]	0.913 0.859	0.921 0.876	0.775 0.700	<u>0.902</u> <u>0.836</u>	0.740 0.660
CFA-Net [14]	0.915 0.861	<u>0.933</u> <u>0.883</u>	0.743 0.665	0.893 0.827	0.732 0.655
I-MedSAM [45]	0.839 0.759	0.871 0.788	0.885 0.800	0.900 0.822	0.874 0.791
SAM2-UNet [12]	<u>0.928</u> <u>0.879</u>	0.907 0.856	0.808 0.730	0.894 0.827	0.796 0.723
FE-UNet (Ours)	0.934 0.889	0.942 0.895	0.830 0.757	0.914 0.852	0.819 0.748

Quantitative Comparison Tables I present quantitative comparisons of typical marine animal segmentation datasets. Compared with CNN-based methods, our method significantly improves performance. On the challenging MAS3K dataset, our method achieves the highest scores across all metrics, delivering a 4-6% improvement. Moreover, our method consistently outperforms others on additional MAS datasets. Compared to state-of-the-art marine animal segmentation models, our model achieves a 1-2% improvement in mIoU and S_α metrics. Compared with Transformer-based methods, our

method achieves a 3-6% improvement on the MAS3K dataset. Furthermore, compared with other SAM-based methods, our model achieves a 1-2% improvement in mIoU scores as well as S_α compared to current SOTA methods.

We follow [64], including the same comparison methods and tools. Table II shows the performance of our model on five polyp segmentation test datasets. On the Kvasir, CVC-ClinicDB, and CVC-300 datasets, our model achieved SOTA performance, with a 1-2% improvement over the second-best method. Furthermore, on the CVC-ColonDB and ETIS datasets, our model demonstrated the second-best segmentation performance.

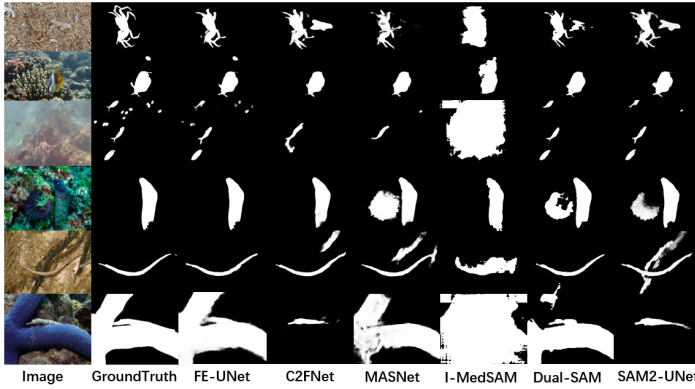
Qualitative Comparison Figures 4 illustrate some visual examples from the marine animal segmentation and polyp segmentation tasks, respectively, to further verify the effectiveness of our method. Compared with previous approaches, our method produces segmentation results that are highly similar to the ground truth in simpler tasks. Moreover, on challenging images with cluttered backgrounds and rich details, our method consistently generates more accurate and refined segmentation masks.

C. Ablation Study

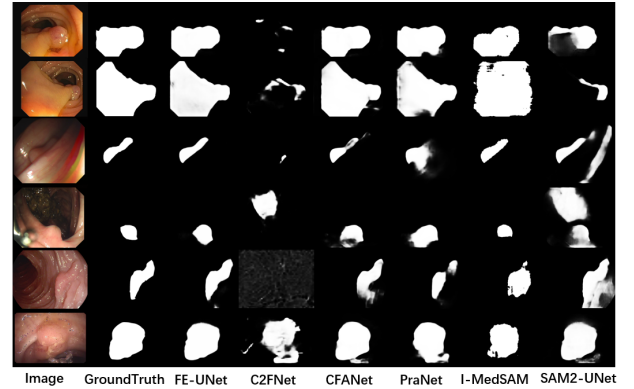
As shown in Figure 5, three ablation experiments on the CVC-300 dataset validated key FE-UNet components. First, ablation within the PFB module showed every element is necessary for optimal performance. Second, replacing FE-UNet’s residual multi-scale extractor with mainstream modules (SPPF [65], SimSPPF [66], SPP [67], ASPP [68], RFB [69]) demonstrated PFB’s superior multi-scale feature extraction. Third, removing PFB, MLP-Adapter, or Res-Adapter individually caused notable performance drops, confirming each component’s indispensability.

V. CONCLUSION

In this work, we propose a novel feature learning framework named FE-UNet for natural image segmentation. Specifically, we introduce the Perceptual Frequency Block (PFB), which aggregates frequency-domain information enhanced by multi-scale WASF modules through the integration of multi-scale



(a) Marine animal segmentation task



(b) Polyp segmentation task

Fig. 4: Qualitative results.

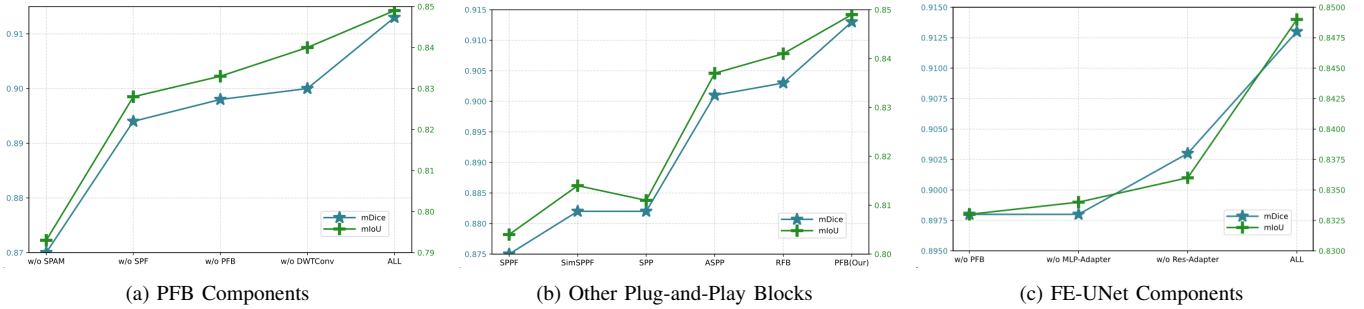


Fig. 5: Visualization of ablation experiment results.

receptive fields and eccentricity-aware mechanisms. This design simulates the human visual system's heightened sensitivity to mid-frequency features, enabling our method to extract rich frequency-domain features critical for fine-grained image segmentation. Experimental results demonstrate state-of-the-art (SOTA) performance in the marine animal segmentation and polyp segmentation task. Our framework is not only applicable to marine animal and medical polyp segmentation scenarios but also lays a solid foundation for image segmentation in other complex scenarios, providing a broader research space for enhancing visual perception capabilities in autonomous robots such as surgical and deep-sea exploration systems.

REFERENCES

- [1] Y. Chen, F. Gao, C. Zhou, X. Yang, X. Xiao, and B. Yan, "Technology and equipment for underwater robots," *Journal of Marine Science and Engineering*, 2025.
- [2] S. Chen, L. Deng, and J. Zhao, "Enhanced reconstruction of satellite-derived monthly chlorophyll a concentration with fourier transform convolutional-lstm," *IEEE TGRS*, pp. 1–14, 2024.
- [3] T. Kitrungsakul, X. Han, Y. Iwamoto, L. Lin, A. H. Foruzan, W. Xiong, and Y. Chen, "Vesselnet: A deep convolutional neural network with multi pathways for robust hepatic vessel segmentation," *Comput. Medical Imaging Graph.*, pp. 74–83, 2019.
- [4] V. Tonkes and M. Sabatelli, "How well do vision transformers (vts) transfer to the non-natural image domain? an empirical study involving art classification," in *ECCV 2022*, 2022, pp. 234–250.
- [5] J. Bai, L. Yuan, S. Xia, S. Yan, Z. Li, and W. Liu, "Improving vision transformers by revisiting high-frequency components," in *ECCV 2022*, 2022, pp. 1–18.
- [6] M. Li, H. Zhang, A. Gruen, and D. L. and, "A survey on underwater coral image segmentation based on deep learning," *GSIS*, pp. 1–25, 2024.
- [7] L. Li, B. Dong, E. Rigall, T. Zhou, J. Dong, and G. Chen, "Marine animal segmentation," *IEEE TCSVT*, pp. 2303–2314, 2022.
- [8] G. Li, Z. Liu, M. Chen, Z. Bai, W. Lin, and H. Ling, "Hierarchical alternate interaction network for RGB-D salient object detection," *IEEE TIP*, pp. 3528–3542, 2021.
- [9] Z. Fu, R. Chen, Y. Huang, E. Cheng, X. Ding, and K.-K. Ma, "Masnet: A robust deep marine animal segmentation network," *IEEE Journal of Oceanic Engineering*, pp. 1104–1115, 2024.
- [10] P. Zhang, T. Yan, Y. Liu, and H. Lu, "Fantastic animals and where to find them: Segment any marine animal with dual SAM," in *CVPR 2024*, 2024, pp. 2578–2587.
- [11] T. Yan, Z. Wan, X. Deng, P. Zhang, Y. Liu, and H. Lu, "MAS-SAM: segment any marine animal with aggregated features," in *IJCAI 2024*, 2024, pp. 6886–6894.
- [12] X. Xiong, Z. Wu, S. Tan, W. Li, F. Tang, Y. Chen, S. Li, J. Ma, and G. Li, "Sam2-UNET: Segment anything 2 makes strong encoder for natural and medical image segmentation," *CoRR*, 2024.
- [13] A. Jafar, Z. U. Abidin, R. A. Naqvi, and S.-W. Lee, "Unmasking colorectal cancer: A high-performance semantic network for polyp and surgical instrument segmentation," *EAAI*, 2024.
- [14] T. Zhou, Y. Zhou, K. He, C. Gong, J. Yang, H. Fu, and D. Shen, "Cross-level feature aggregation network for polyp segmentation," *Pattern Recognit.*, p. 109555, 2023.
- [15] A. He, K. Wang, T. Li, C. Du, S. Xia, and H. Fu, "H2former: An efficient hierarchical hybrid transformer for medical image segmentation," *IEEE TMI*, pp. 2763–2775, 2023.
- [16] F. Wang, X. Sun, and J. Li, "Surgical smoke removal via residual swin transformer network," *Int. J. Comput. Assist. Radiol. Surg.*, pp. 1417–1427, 2023.
- [17] J. W. Cooley, P. A. W. Lewis, and P. D. Welch, "The fast fourier transform and its applications," *IEEE Trans. Educ.*, pp. 27–34, 1969.
- [18] G. Deng and L. Cahill, "An adaptive gaussian filter for noise reduction and edge detection," in *1993 IEEE NSS/MIC*, 1993, pp. 1615–1619 vol.3.

- [19] S. E. Finder, R. Amoyal, E. Treister, and O. Freifeld, "Wavelet convolutions for large receptive fields," in *ECCV 2024*, 2024, pp. 363–380.
- [20] Z. Pan, J. Cai, and B. Zhuang, "Fast vision transformers with hilo attention," in *NeurIPS 2022*, 2022.
- [21] G. Yun, J. Yoo, K. Kim, J. Lee, and D. H. Kim, "Spanet: Frequency-balancing token mixer using spectral pooling aggregation modulation," in *ICCV 2023*, 2023, pp. 6090–6101.
- [22] K. Matkovic, L. Neumann, A. Neumann, T. Psik, and W. Purgathofer, "Global contrast factor - a new approach to image contrast," in *CAE 2005*, 2005, pp. 159–167.
- [23] A. Krizhevsky, "Learning multiple layers of features from tiny images," *University of Toronto*, 05 2012.
- [24] N. Houlsby, A. Giurugi, S. Jastrzebski, B. Morrone, Q. de Laroussilhe, A. Gesmundo, M. Attariyan, and S. Gelly, "Parameter-efficient transfer learning for NLP," in *ICML 2019*, 2019, pp. 2790–2799.
- [25] Z. Qiu, Y. Hu, H. Li, and J. Liu, "Learnable ophthalmology SAM," *CoRR*, 2023.
- [26] J. Wu, R. Fu, H. Fang, Y. Liu, Z. Wang, Y. Xu, Y. Jin, and T. Arbel, "Medical SAM adapter: Adapting segment anything model for medical image segmentation," *CoRR*, 2023.
- [27] S. Rebuffi, H. Bilen, and A. Vedaldi, "Efficient parametrization of multi-domain deep neural networks," in *IEEE CVPR 2018*, 2018, pp. 8119–8127.
- [28] T. Zhao and X. Wu, "Pyramid feature attention network for saliency detection," in *CVPR 2019*, 2019, pp. 3085–3094.
- [29] Z. Wu, L. Su, and Q. Huang, "Stacked cross refinement network for edge-aware salient object detection," in *ICCV 2019*, 2019, pp. 7263–7272.
- [30] Z. Zhou, M. M. R. Siddiquee, N. Tajbakhsh, and J. Liang, "Unet++: Redesigning skip connections to exploit multiscale features in image segmentation," *IEEE TMI*, pp. 1856–1867, 2020.
- [31] X. Qin, Z. Zhang, C. Huang, M. Dehghan, O. R. Zaiane, and M. Jägersand, "U²-net: Going deeper with nested u-structure for salient object detection," *PR*, p. 107404, 2020.
- [32] D. Fan, G. Ji, G. Sun, M. Cheng, J. Shen, and L. Shao, "Camouflaged object detection," in *CVPR 2020*, 2020, pp. 2774–2784.
- [33] Y. Piao, J. Wang, M. Zhang, and H. Lu, "Mfnet: Multi-filter directive network for weakly supervised salient object detection," in *ICCV 2021*, 2021, pp. 4116–4125.
- [34] H. Mei, G. Ji, Z. Wei, X. Yang, X. Wei, and D. Fan, "Camouflaged object segmentation with distraction mining," in *CVPR 2021*, 2021, pp. 8772–8781.
- [35] Y. Lv, J. Zhang, Y. Dai, A. Li, B. Liu, N. Barnes, and D. Fan, "Simultaneously localize, segment and rank the camouflaged objects," in *CVPR 2021*, 2021, pp. 11 591–11 601.
- [36] Y. Sun, G. Chen, T. Zhou, Y. Zhang, and N. Liu, "Context-aware cross-level fusion network for camouflaged object detection," in *IJCAI 2021*, 2021, pp. 1025–1031.
- [37] J. Liu, J. Zhang, and N. Barnes, "Modeling aleatoric uncertainty for camouflaged object detection," in *WACV 2022*, 2022, pp. 2613–2622.
- [38] Y. Pang, X. Zhao, T. Xiang, L. Zhang, and H. Lu, "Zoom in and out: A mixed-scale triplet network for camouflaged object detection," in *CVPR 2022*, 2022, pp. 2150–2160.
- [39] S. Zheng, J. Lu, H. Zhao, X. Zhu, Z. Luo, Y. Wang, Y. Fu, J. Feng, T. Xiang, P. H. S. Torr, and L. Zhang, "Rethinking semantic segmentation from a sequence-to-sequence perspective with transformers," in *CVPR 2021*, 2021, pp. 6881–6890.
- [40] J. Chen, Y. Lu, Q. Yu, X. Luo, E. Adeli, Y. Wang, L. Lu, A. L. Yuille, and Y. Zhou, "Transunet: Transformers make strong encoders for medical image segmentation," *CoRR*, 2021.
- [41] A. Kirillov, E. Mintun, N. Ravi, H. Mao, C. Rolland, L. Gustafson, T. Xiao, S. Whitehead, A. C. Berg, W. Lo, P. Dollár, and R. B. Girshick, "Segment anything," in *ICCV 2023*, 2023, pp. 3992–4003.
- [42] J. Wu, R. Fu, H. Fang, Y. Liu, Z. Wang, Y. Xu, Y. Jin, and T. Arbel, "Medical SAM adapter: Adapting segment anything model for medical image segmentation," *CoRR*, 2023.
- [43] T. Chen, L. Zhu, C. Ding, R. Cao, Y. Wang, Z. Li, L. Sun, P. Mao, and Y. Zang, "SAM fails to segment anything? - sam-adapter: Adapting SAM in underperformed scenes: Camouflage, shadow, and more," *CoRR*, 2023.
- [44] Y. Lai, Z. Luo, and Z. Yu, "Detect any deepfakes: Segment anything meets face forgery detection and localization," in *CCBR 2023*, 2023, pp. 180–190.
- [45] X. Wei, J. Cao, Y. Jin, M. Lu, G. Wang, and S. Zhang, "I-medsam: Implicit medical image segmentation with segment anything," in *ECCV 2024*, 2024, pp. 90–107.
- [46] J. Yang, C. Li, X. Dai, and J. Gao, "Focal modulation networks," in *NeurIPS 2022*, 2022.
- [47] D. Jha, P. H. Smedsrud, M. A. Riegler, P. Halvorsen, T. de Lange, D. Johansen, and H. D. Johansen, "Kvasir-seg: A segmented polyp dataset," in *MMM 2020*, 2020, pp. 451–462.
- [48] J. Bernal, F. J. Sánchez, G. Fernández-Esparrach, D. Gil, C. R. de Miguel, and F. Vilarinho, "WM-DOVA maps for accurate polyp highlighting in colonoscopy: Validation vs. saliency maps from physicians," *Comput. Medical Imaging Graph.*, pp. 99–111, 2015.
- [49] N. Tajbakhsh, S. R. Gurudu, and J. Liang, "Automated polyp detection in colonoscopy videos using shape and context information," *IEEE TMI*, pp. 630–644, 2016.
- [50] D. Vázquez, J. Bernal, F. J. Sánchez, G. Fernández-Esparrach, A. M. López, A. Romero, M. Drozdal, and A. C. Courville, "A benchmark for endoluminal scene segmentation of colonoscopy images," *CoRR*, 2016.
- [51] J. Silva, A. Histace, O. Romain, X. Dray, and B. Granado, "Toward embedded detection of polyps in WCE images for early diagnosis of colorectal cancer," *Int. J. Comput. Assist. Radiol. Surg.*, pp. 283–293, 2014.
- [52] O. Ronneberger, P. Fischer, and T. Brox, "U-net: Convolutional networks for biomedical image segmentation," in *MICCAI 2015*, 2015, pp. 234–241.
- [53] Y. Fang, C. Chen, Y. Yuan, and R. K. Tong, "Selective feature aggregation network with area-boundary constraints for polyp segmentation," in *MICCAI 2019*, 2019, pp. 302–310.
- [54] D. Fan, G. Ji, T. Zhou, G. Chen, H. Fu, J. Shen, and L. Shao, "Pranet: Parallel reverse attention network for polyp segmentation," in *MICCAI 2020*, 2020, pp. 263–273.
- [55] K. Patel, A. M. Bur, and G. Wang, "Enhanced u-net: A feature enhancement network for polyp segmentation," in *CRV 2021*, 2021, pp. 181–188.
- [56] J. Wei, Y. Hu, R. Zhang, Z. Li, S. K. Zhou, and S. Cui, "Shallow attention network for polyp segmentation," in *MICCAI 2021*, 2021, pp. 699–708.
- [57] X. Zhao, L. Zhang, and H. Lu, "Automatic polyp segmentation via multi-scale subtraction network," in *MICCAI 2021*, 2021, pp. 120–130.
- [58] T. Liao, C. Yang, Y. Lo, K. Lai, P. Shen, and Y. Lin, "Hardnet-dfus: Enhancing backbone and decoder of hardnet-mseg for diabetic foot ulcer image segmentation," in *MICCAI 2022*, 2022, pp. 21–30.
- [59] Z. Yin, K. Liang, Z. Ma, and J. Guo, "Duplex contextual relation network for polyp segmentation," in *ISBI 2022*, 2022, pp. 1–5.
- [60] R. Zhang, P. Lai, X. Wan, D. Fan, F. Gao, X. Wu, and G. Li, "Lesion-aware dynamic kernel for polyp segmentation," in *MICCAI 2022*, 2022, pp. 99–109.
- [61] T. Zhou, Y. Zhou, C. Gong, J. Yang, and Y. Zhang, "Feature aggregation and propagation network for camouflaged object detection," *IEEE TIP*, pp. 7036–7047, 2022.
- [62] R. Zhang, G. Li, Z. Li, S. Cui, D. Qian, and Y. Yu, "Adaptive context selection for polyp segmentation," *CoRR*, 2023.
- [63] A. Lou, S. Guan, and M. H. Loew, "Caranet: Context axial reverse attention network for segmentation of small medical objects," *CoRR*, 2023.
- [64] T. Zhou, Y. Zhang, Y. Zhou, Y. Wu, and C. Gong, "Can SAM segment polyps?" *CoRR*, 2023.
- [65] R. Khanam and M. Hussain, "What is yolov5: A deep look into the internal features of the popular object detector," *CoRR*, 2024.
- [66] C. Li, L. Li, H. Jiang, K. Weng, Y. Geng, L. Li, Z. Ke, Q. Li, M. Cheng, W. Nie *et al.*, "Yolov6: A single-stage object detection framework for industrial applications," *CoRR*, 2022.
- [67] K. He, X. Zhang, S. Ren, and J. Sun, "Spatial pyramid pooling in deep convolutional networks for visual recognition," *IEEE TPAMI*, pp. 1904–1916, 2015.
- [68] L. Chen, G. Papandreou, I. Kokkinos, K. Murphy, and A. L. Yuille, "Deeplab: Semantic image segmentation with deep convolutional nets, atrous convolution, and fully connected crfs," *IEEE TPAMI*, pp. 834–848, 2018.
- [69] S. Liu, D. Huang, and Y. Wang, "Receptive field block net for accurate and fast object detection," in *ECCV 2018*, V. Ferrari, M. Hebert, C. Sminchisescu, and Y. Weiss, Eds., 2018, pp. 404–419.